Detailed TIMS Study of Ar/C_2H_2 Expanding Thermal Plasma: Identification of a-C:H Film Growth Precursors

J. Benedikt,[†] D. C. Schram, and M. C. M. van de Sanden*

Department of Applied Physics, Eindhoven University of Technology, Eindhoven, The Netherlands

Received: May 19, 2005; In Final Form: August 26, 2005

Acetylene chemistry is studied by means of threshold ionization mass spectrometry (TIMS) in remote Ar/C_2H_2 expanding thermal plasma to identify the growth precursors of hydrogenated amorphous carbon (a-C:H) films. More than 20 hydrocarbon species are measured, enabling a comprehensive study of acetylene chemistry in the plasma environment. It is shown that the plasma composition is controlled by the initial ratio between the acetylene flow into the reactor and argon ion and electron fluence emanating from the remote plasma source. Complete decomposition of acetylene to C, CH, CH_2, C_2, and C_2H radicals is achieved in subsequent charge transfer and dissociative recombination reactions under low acetylene flow conditions. The formation of soft polymer-like a-C:H films can be attributed to C, C_2, and also partially to CH and C_2H deposition. At acetylene flows higher than argon ion and electron fluence, reactions of C, CH, C_2, and C_2H radicals with acetylene lead to the formation of various hydrocarbon species, whose behavior is dependent on whether the number of carbon atoms is even or odd. The detected resonantly stabilized C_3, C_3H, and probably also C_5 and C_5H radicals are unreactive with acetylene in the gas phase and are, therefore, abundantly present close to the substrate. The C_3 radical has among them the highest density, and it is identified as the significant growth precursor of Ar/C_2H_2 expanding thermal plasma deposited hard a-C:H films.

1. Introduction

Diamondlike carbon (DLC) films have been attracting attention since their first preparation by Aisenberg and Chabot in 1971,[1] mostly for their superior mechanical, optical, chemical, and electronic properties. Moreover, these properties can be easily tuned to desired values by tuning the process parameters. DLC is a metastable amorphous material usually characterized by a hydrogen content [hydrogenated DLCs are called hydrogenated amorphous carbon (a-C:H)] and a ratio between sp^2 and sp^3 bonded carbon. Research over the years has established that the sp^2 phase is responsible for optical and electronic properties and the sp^3 phase determines to a large extent the mechanical properties.[2] DLCs are used as protective coatings on magnetic storage disks, IR optic elements, or razor blades,[3,4] and if doped, for example, with nitrogen, they can be used as electronic thin films in cold cathode field emission displays or electrode materials in electrochemical studies of water treatments.[5] Recently, it was shown that a-C:H, in which orientational order has been induced by directional irradiation with a low energy ion beam, can be used for liquid crystal alignment in liquid crystal display processing.[6,7] Non-hydrogenated DLCs have also a potential application in poly-light-emitting diode (LED) and organic-LED devices.[8,9]

DLC can be prepared by various deposition techniques such as ion beam deposition, sputtering, pulsed laser deposition, and plasma enhanced chemical vapor deposition (PECVD) with different hydrocarbon gases.[2] DLC is also formed on the surface in the divertor and other inner parts of the fusion devices as a result of erosion of graphite tails and redeposition of C_xD_y and C_xT_y species. To achieve optimal mechanical and structural properties, ion bombardment of the growing film with ion energies in excess of about 100 eV is usually involved. The role of energetic ions in the deposition process of DLC is already well understood: they penetrate into the subsurface region and displace hydrogen and carbon atoms, which leads to an enhanced cross-linking of the carbon network and to hydrogen removal from the growing film, resulting in dominant sp^3 bonded film structure.[10]

It was shown that a-C:H films having good mechanical and structural properties (e.g., hardness up to 14 GPa) can be prepared in the absence of ion bombardment by means of a remote Ar/C_2H_2 expanding thermal plasma (ETP). Moreover, very high deposition rates up to 70 nm/s can be achieved with film quality, in terms of hardness, improving as the growth rate increases,[11,12] which makes it an attractive deposition technique for industry. Radicals rather than energetic ions dominate the growth in this type of plasma.

In general, the role of radicals in the growth process of DLC films is not well understood, mainly due to the complexity of the processes involved. For example, the growth can depend on the hydrogen passivation of the a-C:H surface, the deposition temperature (surface diffusion, bond stability, etc.), and the radical fluxes toward the surface. Moreover, numerous particles can be involved; even when simple CH_4 or C_2H_2 gas precursors are used, a plethora of hydrocarbon radicals and stable species is formed. The detection and measurement of radicals, for example, by laser spectroscopy, under plasma conditions is difficult and limited by their usual low densities. Understanding the plasma chemistry of Ar/C_2H_2 ETP, identification of the growth precursors and unraveling the growth mechanism can provide, therefore, valuable information for other fields in which hydrocarbon chemistry and radicals are involved: DLC deposition, combustion of hydrocarbon gases, plasma−divertor inter-

---

* Corresponding author. E-mail: m.c.m.v.d.sanden@tue.nl.

[†] E-mail: jan.benedikt@rub.de. Current address: Department of Physics and Astronomy, Ruhr-University Bochum, Bochum, Germany.

10.1021/jp052623a CCC: $30.25

action in fusion devices, or the formation of hydrocarbon species in interstellar environments.

From mass spectrometry and Langmuir probe measurements, it was previously established that Ar/C_2H_2 ETP chemistry is dominated by argon ion induced dissociation of the injected C_2H_2.[13] Furthermore, cavity ringdown absorption spectroscopy (CRDS) measurements of carbon (C), methylidyne (CH), and dicarbon (C_2) radicals, formed in the dissociative recombination (DR) of a C_2H_2 ion with an electron, led to the conclusion that the contribution of these species to the growth of hard a-C:H films is, under high rate deposition conditions, negligible.[14−16] A residual gas analyzer (RGA) was also used to monitor stable plasma chemistry products in the plasma background. The diacetylene molecule (C_4H_2), which is formed in the reaction of ethynyl radical (C_2H) with C_2H_2, was observed with a high density.[17] On the basis of these results, it was hypothesized that the C_2H has only a minor contribution to growth under high rate deposition conditions. These studies have revealed that the plasma chemistry is more complex than originally anticipated[13,18,19] and that some additional so far undetected species must be present in the Ar/C_2H_2 ETP and contribute to the a-C:H film growth.

In this article, we apply the threshold ionization mass spectrometry (TIMS) diagnostic technique to detect diverse hydrocarbon radicals, to understand the plasma chemistry, and to identify the growth precursors in an Ar/C_2H_2 ETP. TIMS is capable of the detection of a variety of low density reactive species at the position of the substrate without the limitations inherent to some of the optical techniques, such as the existence of suitable optical transitions of the radical or the molecule of interest, and it has already been used in our group to detect SiH_3, SiH_2, and N radicals in an Ar/H_2(/N_2)/SiH_4 ETP.[20,21] Here, we report the detection of more than 20 hydrocarbon radicals and molecules in the Ar/C_2H_2 ETP. The absolute density measurements of these species allowed us to draw conclusions about their role in the growth mechanism of a-C:H films.

2. Experimental Setup

Figure 1 shows schematically the ETP setup.[18] The thermal argon plasma is formed in the so-called cascaded arc at a gas pressure of approximately 0.2−0.5 bar. The electron temperature in the plasma is similar to heavy species temperature with the value $T_e \sim T_h \sim 1$ eV.[22] The cascaded arc operation is controlled by argon flow and arc dc current. A constant value of 100 sccs (standard cubic centimeters per second, 1 sccs $= 2.69 \times 10^{19}$ particles/s) of argon flow and an arc current in the range of 22−61 A was used for the measurements presented in this article. The thermal argon plasma expands into the low pressure vessel. The expansion is supersonic until going through a stationary shock at approximately 5 cm from the nozzle, after which it is subsonic. T_e drops in the expansion to values less than 0.3 eV.[23] The pressure difference between the cascaded arc and the vessel makes the plasma production remote and the arc operation independent of the conditions in the expansion vessel.

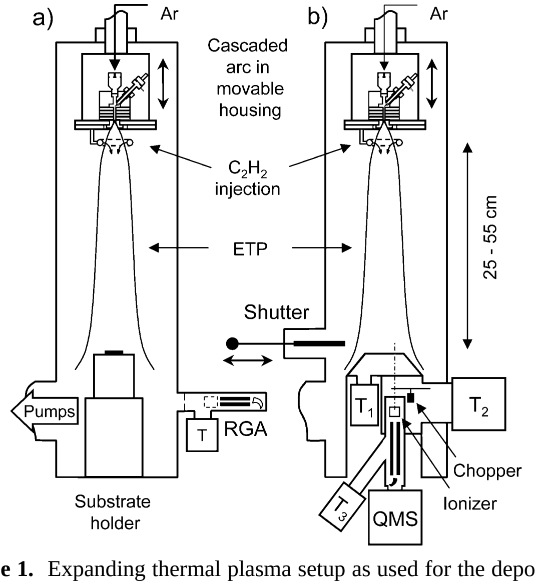

Figure 1. Expanding thermal plasma setup as used for the deposition (a) with the installed residual gas analyzer (RGA) and the same setup with the implemented quadrupole mass spectrometer (QMS) with the three differential pumping stages (b).

The C_2H_2 is admixed into the ETP by means of the injection ring located approximately at the position of the stationary shock. The Ar/C_2H_2 ETP flows from this point at a subsonic speed toward the substrate with a transport time from the injection ring to the substrate in the order of a millisecond. The cascaded arc is enclosed in a movable housing, which allows variation of the injection ring−substrate plane distance in the range 25−55 cm (and hence also changing the transport time). The vessel pressure is kept constant at 29 Pa by means of additional argon injection into the plasma background through a leak valve. The base pressure in the experimental chamber is maintained by a 1000 L/s turbo pump and is below 10^{-6} mbar. During the plasma operation two mechanical booster pumps are used with a total pumping capacity of 400 L/s. The a-C:H films are deposited on a temperature-controlled substrate (c-Si, Al, glass, ...) typically at 250 °C.[18] The ion bombardment of the substrate can be neglected because only a small self-bias (<2 V) is present on the substrate, a consequence of the low electron temperature. The growth is monitored by in situ single wavelength real-time ellipsometry (HeNe laser, 632.8 nm, not shown in Figure 1), which provides information about the growth rate, refractive index, and extinction coefficient of the growing film.[24] Figures 2 and 3 show the growth flux in carbon atoms/(s m^2) and film refractive index as a function of two process parameters, the C_2H_2 gas flow and the arc current. Both growth flux and refractive index increase with increasing arc current and C_2H_2 flow. The growth flux is calculated from the growth rate multiplied by the film density, determined from its previously established relation with the refractive index.[11] The maximum growth flux measured at an arc current of 61 A and a C_2H_2 flow of 18 sccs corresponds to a growth rate of

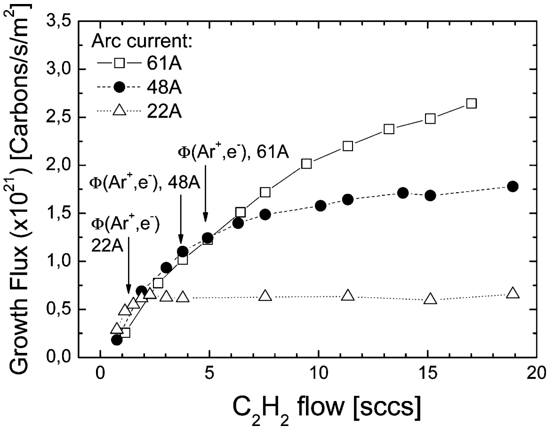

Figure 2. Growth flux in carbon atoms/(s m^2) measured at a substrate temperature of 250 °C. The arrows indicate the argon ion and electron fluence for every arc current.

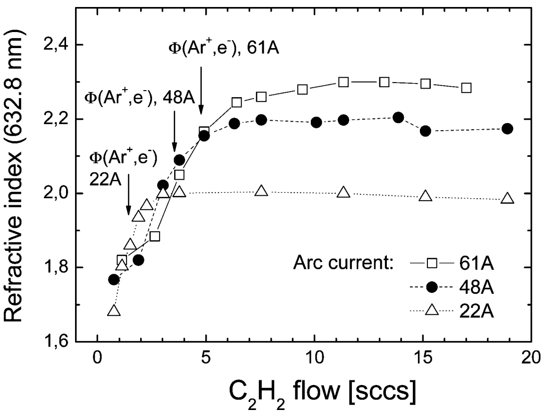

Figure 3. Refractive index at 632.8 nm measured at a substrate temperature of 250 °C. The arrows indicate the argon ion and electron fluence for every arc current.

30 nm/s. Films deposited under these conditions have a hardness of 14 GPa, a Young's modulus of 120 GPa, and a density of 1.65 g/cm^3. They can be classified as medium hard DLC films.

The substrate holder is replaced by a three-stage molecular beam TIMS (Hiden Analytical EPIC 300, PSM upgrade) setup to measure the neutral species densities at the substrate plane.[25] The plasma is sampled through a 0.8-mm-diameter orifice, which is in line of sight with the quadrupole mass spectrometer (QMS) ionizer. The QMS itself was situated in the third stage of the three-stage differentially pumped stainless steel housing. The pressure in the third stage during plasma operation was below 2×10^{-7} mbar. A mechanical chopper is placed in the second stage of the differential pumping to modulate the molecular beam, formed after the sampling orifice, and to separate the signal due to the particles in the molecular beam from the background species that are present in the QMS ionizer. An additional correction has to be taken into account for the background pressure variation in the third stage at the moment the chopper position is changed. The TIMS setup and the density calibration procedure are treated in great detail elsewhere.[25] It was not always possible to perform a proper background correction in the density calibration procedure. For radical species with low reaction probability on a stainless steel surface (expected, e.g., for CH_2 or CH_3 radicals), the background pressure can build up inside the stainless steel housing of the QMS and background species can contribute up to 50% of the measured signal.[25] Therefore, the calibration procedure provides only an upper density limit for these species, which can be overestimated up to a factor of 2. For radicals with a surface reaction probability close to unity (e.g., C, C_2, CH, or C_2H), no background correction is needed, leading to reliable density measurements. Furthermore, in the calibration procedure, knowledge of the electron impact ionization cross section is necessary. However, they are not available for most of the hydrocarbon species detected and they have to be estimated. On the basis of the similar near-threshold electron impact ionization cross-sectional behavior, measured for several hydrocarbon species, unknown cross sections are approximated by the cross section of the C_2H_2 molecule. The unknown electron impact ionization cross section is the main source of systematic error in the calculation of radical densities.[25]

3. Plasma Chemistry

The ETP can be represented to a good approximation by a plug-down geometry in which the (forward) plasma chemistry evolves along the expansion axis, starting at the injection ring, where C_2H_2 is admixed to the argon ETP, and is terminated after the transport time (~1 ms) at the substrate holder, where reactive radicals such as C, CH, C_2, C_2H, C_3, C_3H, and C_5 deposit and only radicals with a low surface reactivity (e.g., CH_2) or stable molecules, such as C_4H_2, get into the plasma background. The beam directed (drift) velocity was measured by Engeln et al.,[26] and it is around 2000 m/s at the position of the injection ring (after the stationary shock) and drops to values below 200 m/s close to the substrate plane, at 55 cm from the ring. The stable plasma chemistry products circulate in the plasma background (with a recirculation time of ~10 ms) and can diffuse back into the main plasma stream and react there or are finally pumped away (with a typical residence time of ~400 ms). The barrel shock around the supersonic expansion region limits direct injection of the background recirculating species into the ETP. Furthermore, recombination of, for example, atomic hydrogen takes place at the reactor wall and the pyrolysis of the stable molecules can occur on the electron and plasma-heated arc nozzle or other hot parts of the setup (cf. Figure 4). However, despite these additional phenomena, the results presented in this article confirm that the forward plasma chemistry determines the plasma composition near the substrate plane.

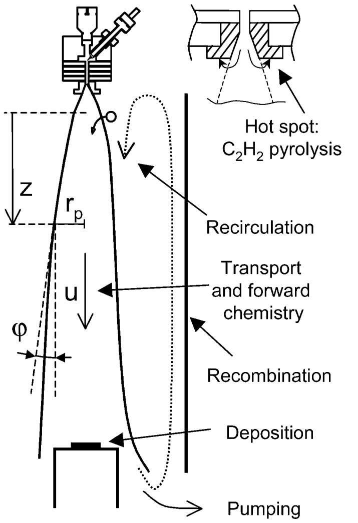

Figure 4. Schematic illustrating different processes in expanding thermal plasma together with the parametrization of the expanding beam used in the plasma chemistry simulation model (cf. the Appendix).

The primary dissociation of C_2H_2 is argon ion induced and proceeds through a charge transfer (CT) reaction between the Ar ion and the C_2H_2 molecule,[27] reaction R1 in Table 1, followed by a fast DR reaction of the $C_2H_2^+$ ion with an electron, reactions R2a–R2e in Table 1. The electron impact induced dissociation and ionization processes can be neglected due to the low electron temperature.[28] The branching ratio of the DR reactions R2a–R2e, involving the ground state $C_2H_2^+$ ion, was measured in an ion storage ring experiment.[29] Next to these primary CT and DR reactions, secondary CT and DR reaction steps are also possible, which will dissociate primary reaction products using an additional argon ion and electron pair (cf. reactions R3–R10). The branching ratios of these reactions were not measured, and values estimated by Janev et al.[30,31] are adopted here. Also, the reaction rates for DR reactions are calculated as proposed by Janev et al., with $T_e = 0.3$ eV (as determined from Thomson–Rayleigh scattering[32] and Langmuir probe[22] measurements). The secondary CT and DR reactions R3–R10 will compete with radical–neutral reactions of primary

TABLE 1: Charge Transfer and Dissociative Recombination Reactions

no.	reaction channel		k (cm^3/s)	reaction yields[a]	ref
R1	$Ar^+ + C_2H_2$	$\rightarrow C_2H_2^+ + Ar$	$(4.2 \pm 1.4) \times 10^{-10}$	1	*b*
R2a	$C_2H_2^+ + e^-$	$\rightarrow C_2H + H$	9.5×10^{-8}	0.50[c]	*d,e*
R2b		$\rightarrow C_2 + H + H$		0.30[c]	
R2c		$\rightarrow CH + CH$		0.13[c]	
R2d		$\rightarrow CH_2 + C$		0.05[c]	
R2e		$\rightarrow C_2 + H_2$		0.02[c]	
R3	$Ar^+ + C_2H$	$\rightarrow C_2H^+ + Ar$	k_{R1}	1	estimated
R4a	$C_2H^+ + e^-$	$\rightarrow C_2 + H$	7.2×10^{-8}	0.47	*e*
R4b		$\rightarrow C + CH$		0.38	
R4c		$\rightarrow C + C + H$		0.15	
R5	$Ar^+ + C_2$	$\rightarrow C_2^+ + Ar$	k_{R1}	1	estimated
R6	$C_2^+ + e^-$	$\rightarrow C + C$	6×10^{-8}	1	estimated
R7	$Ar^+ + CH$	$\rightarrow CH^+ + Ar$	k_{R1}	1	estimated
R8	$CH^+ + e^-$	$\rightarrow C + H$	4.5×10^{-8}	1	*f*
R9	$Ar^+ + CH_2$	$\rightarrow CH_2^+ + Ar$	k_{R1}	1	estimated
R10a	$CH_2^+ + e^-$	$\rightarrow CH + H$	5.2×10^{-8}	0.25	*f*
R10b		$\rightarrow C + H_2$		0.12	
R10c		$\rightarrow C + H + H$		0.63	

[a] Reaction yields as reported in the literature. [b] Reference 27. [c] Different reaction yields are used in the simulation model. More details can be found in the text. [d] Reference 29. [e] Reference 31. [f] Reference 30.

TABLE 2: Radical−Neutral Reactions

no.	reaction channel		reaction yields used	$k \times 10^{-10}$ (cm^3/s)	Δ_rH (eV)	ref
R11a	$C + C_2H_2$	$\rightarrow C_3H + H$	0	2.7	−0.80/−0.86[a]	*b−e*
R11b		$\rightarrow C_3 + H_2$	1		−1.28/−0.43[a]	
R12a	$CH + C_2H_2$	$\rightarrow C_3H_2 + H$	0	2.0	−0.83[f]	*c,g*
R12b		$\rightarrow C_3H + H_2$	1		−1.91/−1.86[a]	
R12c		$\rightarrow C_3 + H + H_2$	0		2.25/3.10[a]	
R13	$CH_2 + C_2H_2$	$\rightarrow C_3H_3 + H$	1	3.0	−0.56	*c*
R14a	$C_2 + C_2H_2$	$\rightarrow C_4H + H$	0.5	2.7	−0.42	*h,i*
R14b		$\rightarrow C_4 + H_2$	0.5		−0.97	
R14c		$\rightarrow C_2H + C_2H$	0		−1.15/0.49[j]	
R14d		$\rightarrow CH_2 + C_3$	0		1.47/2.32[a]	
R14e		$\rightarrow C_3H_2 + C$	0		1.82[f]	
R14f		$\rightarrow C_3H + CH$	0		1.79/1.73[a]	
R15a	$C_2H + C_2H_2$	$\rightarrow C_4H_2 + H$	1	1.3	−0.22/−1.04[j]	*k*
R15b		$\rightarrow C_4H + H_2$	0		0.82/0.00[j]	
R16	$C + C_4H_2$	$\rightarrow C_5H + H$	0	5.2		estimated
		$\rightarrow C_5 + H_2$	1			
R17	$CH + C_4H_2$	$\rightarrow C_5H_2 + H$	0	3.6		estimated
		$\rightarrow C_5H + H_2$	1			
		$\rightarrow C_5 + H_2 + H$	0			
R18	$C_2 + C_4H_2$	$\rightarrow$?		5.4		estimated
R19	$C_2H + C_4H_2$	$\rightarrow C_6H_2 + H$	1	3.3		*l*
R20	$C_4H + C_2H_2$	$\rightarrow C_6H_2 + H$	1	1.0		estimated
R21	$C_4 + C_2H_2$	$\rightarrow$?		3.5		estimated

[a] Values are for linear and cyclic isomers, respectively. [b] Reference 51. [c] Kaiser, R. I.; Ochsenfeld, C.; Head-Gordon, M.; Lee, Y. T.; Suits, A. G. *Science* **1996**, *274*, 1508. [d] Guadagnini, R.; Shatz, G. C.; Walch, S. P. *J. Phys. Chem. A* **1998**, *102*, 5857. [e] Chastaing, D.; Le Picard, S. D.; Sims, I. R.; Smith, I. W. M. *Astron. Astrophys.* **2001**, *365*, 241. [f] For cyclopropenylidene, cyc-C_3H_2. [g] Thiesemann, H.; MacNamara, J.; Taaties, C. A. *J. Phys. Chem. A* **1997**, *101*, 1881. [h] Reference 43. [i] Reisler, H.; Mangir, M. S.; Wittig, C. *J. Chem. Phys.* **1980**, *75*, 2280 (different reactivities for triplet and singlet C_2 are reported, average value is used). [j] Two different values for the enthalpy of formation of C_2H are available (cf. ref 56). [k] Reference 40. [l] Nizamov, B.; Leone, S. R. *J. Phys. Chem. A* **2004**, *108*, 1746.

reaction products with C_2H_2 and other stable plasma chemistry products, as listed in Table 2. The initial flow ratio between the C_2H_2 flow injected through the ring and the argon ion and electron fluence emanating from the cascaded arc, here defined as $F = \Phi(C_2H_2)/\Phi(Ar^+,e^-)$, is the critical parameter, which determines whether CT and DR reactions ($F < 1$) or radical−neutral reactions ($F > 1$) will dominate the forward plasma chemistry after the primary C_2H_2 decomposition. The argon ion and electron fluence $\Phi(Ar^+,e^-)$ is dependent on the arc current and has values of 1.3, 3.5, and 4.8 sccs for 22, 48, and 61 A, respectively. The radical−radical reactions will have a marginal effect on the plasma composition, since the radical densities are much smaller than stable product densities such as C_2H_2 and C_4H_2, and they can be in the first approximation neglected.

Plasma Chemistry Simulation Model. We built a numerical quasi-one-dimensional plasma chemistry simulation model to test the plasma chemistry as discussed above and compare it with the experimental results. The model is based on the particle conservation equations for the species number density along the expansion axis, taking into account the influence of the species-dependent radial diffusion. Since the C_2H_2 is injected at the position of the stationary shock front, only the subsonic part of the plasma is taken into account following the approach used by Kroesen et al.[33] or van de Sanden et al.[23]

The model provides the species averaged number densities across the beam at given distances from the injection ring assuming (to the first approximation) that the directed velocity is constant (1000 m/s) along the subsonic part of the expansion. The argon ion and electron fluence together with the ETP beam radius at the injection ring are used as fitting parameters to optimize the model output. The model details can be found in the Appendix.

4. Results and Discussion

The radical measurements are performed as a function of the C_2H_2 flow at an arc current of 48 A. The radicals are detected at two arc positions: at injection ring−substrate plane distances of 25 and 55 cm. The 55 cm distance is the same as the one used during the deposition (cf. Figure 1), and experimental results obtained at this distance can be directly related to the film growth rate and film properties. The measurements with the arc lowered to an injection ring−substrate plane distance of 25 cm are performed to probe the evolution of the plasma composition along the expansion axis. However, when the arc is lowered, the flow pattern in the reactor is changed, which can have an influence on the plasma chemistry as well. To evaluate how large this effect is, the CH radical measurements by TIMS (13 amu, at injection ring−substrate plane distances of 25 and 55 cm) and CRDS are compared in Figure 5. The CRDS measurements were performed with a fixed injection ring−substrate plane distance of 55 cm (Figure 1a) and with the laser beam crossing the expansion axis at distances of 25 and 52 cm from the injection ring, with the latter one being 3 cm above the substrate plane.[17]

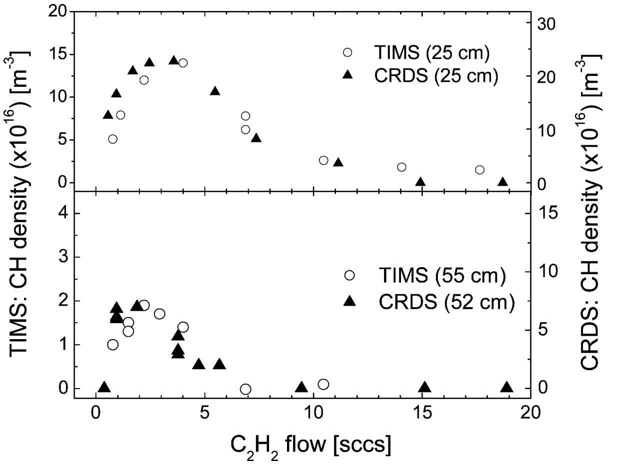

Figure 5. Comparison between CH radical density as measured by TIMS and CRDS experimental techniques.

The relative TIMS and CRDS measurements of CH are in good agreement at both positions, confirming that there is only a marginal change in the relative density of measured species as a function of the C_2H_2 flow. Comparison of absolute values, or at least the difference between 25 cm and 55 (52) cm for these two experimental techniques is more difficult for several reasons. Since CRDS utilizes the light absorption, it measures line-of-sight densities, so the length of the absorption path has to be assumed and it is a possible source of errors in the density calculation. We used 10 and 20 cm absorption path lengths at 25 and 52 cm, respectively, to calculate the CH density.[14] Additionaly, the fact that the CRDS measurement is performed 3 cm above the substrate and not in the substrate plane can lead to a difference between TIMS and CRDS measurements. It was discussed[34,35] that the density of the reactive species with nonzero surface reaction probability decreases as the distance to the surface decreases. The density gradient near the surface and the density at the surface depend on the surface reaction probability as well as on the conditions near the surface, which will be in our case determined mainly by the flow stagnation region formed above the substrate. The flow stagnation region is changed when the arc housing is lowered because the ETP beam directed velocity is higher at shorter distances from the arc nozzle.[26] The change of the stagnation region can explain the different ratio between the CRDS and TIMS measurements at 25 and 55 (52) cm. Moreover, the TIMS housing has a bigger diameter (∼15 cm) than the original substrate holder (∼11 cm), which can result in a changed flow pattern even at 55 cm compared to the CRDS experiments, which were performed with the original substrate holder. Taking all of these effects into account, one can see that the absolute CH densities measured by TIMS and CRDS also agree reasonably well.

The further discussion in this section is organized as follows. First, the measurements of primary CT and DR reaction products (the C, CH, CH_2, C_2, and C_2H radicals) are shown and the plasma chemistry and contribution of these species to the growth under $F < 1$ conditions are discussed. Next, the measurements of the secondary reaction products (the C_3, C_3H, C_3H_2, C_4, C_4H, and C_4H_2 species), which are formed in the reactions of C_2H_2 with primary reaction products, are presented and their possible role in the growth is discussed. Finally, the results related to C_5, C_5H, C_6H_2, C_6H_6, and some other species, identified as minor background species not relevant to the growth mechanism, are shown.

Primary Reaction Products. Plasma chemistry starts with C_2H_2 decomposition in primary reactions R1 and R2a−R2e. The relative yields and gas phase reactivity of the primary reaction products (C, CH, CH_2, C_2, and C_2H) determine the subsequent plasma chemistry and plasma composition. Therefore, the measurements of these radicals are reported first.

C_2H and CH_2. Figures 6 and 7 show the measurement of C_2H and CH_2 radicals as a function of the C_2H_2 flow together with the simulated densities. The maximum densities at 55 cm were determined to be $4.0^{+3.5}_{-2.5} \times 10^{16}$ and $1.3^{+1.1}_{-0.8} \times 10^{16}$ m^{-3} for C_2H and CH_2, respectively, but as already explained, the CH_2 density can be overestimated up to a factor of 2 due to its expected low surface reaction probability (possible error in the background correction during the TIMS measurement[25]). The measured densities are a result of the C_2H and CH_2 production

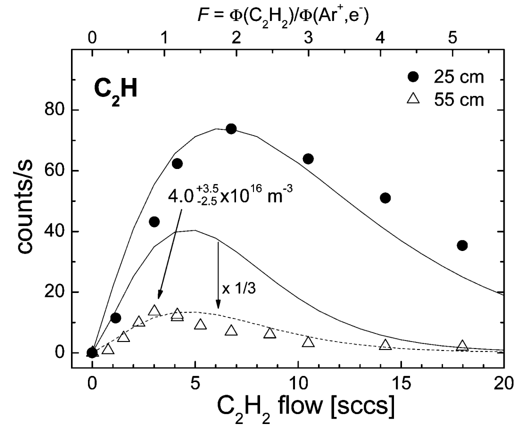

Figure 6. TIMS C_2H radical measurement together with the simulated results (lines).

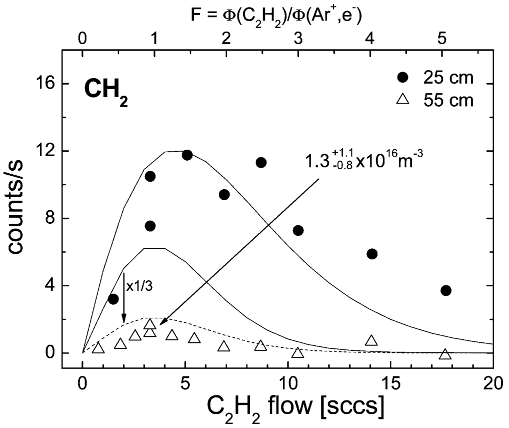

Figure 7. TIMS CH_2 radical measurement together with the simulated results (lines).

and loss processes in the plasma chemistry. Both radicals have first-order behavior, since they are predominantly produced in the primary CT and DR reactions R1 and R2. The dominant loss processes are due to reactions with C_2H_2 ($F > 1$) or secondary CT and DR reactions ($F < 1$). The maximum at 55 cm is measured at $F \sim 1$ (C_2H_2 flow of 3.5 sccs), as expected for dominant primary reaction products, since all argon ions, electrons, and C_2H_2 molecules needed in loss processes are equally depleted in reactions R1 and R2. The agreement between simulated and measured relative densities as a function of C_2H_2 flow confirms the primary nature of C_2H and CH_2 radicals in Ar/C_2H_2 ETP.

As can be seen in Figures 6 and 7, the model predicts a smaller difference between the densities at 25 and 55 cm than that determined by TIMS. Moreover, the simulated densities are approximately 5 times higher than the measured densities. (The absolute values of simulated densities are not shown in these and following figures, and the model results are rescaled to the experimental data.) As already mentioned when we discussed the difference between the CRDS and TIMS measurements, these differences can be attributed to the decrease of the density of the reactive species in the vicinity of the surface as well as the change of the flow stagnation region, when the arc housing is lowered. When the simulated results for 55 cm are rescaled by a factor of $^1/_3$, good agreement between the simulation model and the measured data is achieved for most of the species. In the rest of this article, simulation results at 55 cm are rescaled by $^1/_3$.

C, CH, and C_2. C, CH, and C_2 are the remaining possible primary reaction products, and their measurements as a function of the C_2H_2 flow are shown in Figures 8, 9, and 10, respectively. The density behavior of these radicals is different from that of C_2H and CH_2 due to secondary CT and DR reactions R3–R6. These reactions are also sources of C, CH, and C_2 radicals. Additional argon ion and electron pairs are needed for these reactions, and hence, C, CH, and C_2 radicals have a maximum density at $F < 1$, even at the 25 cm distance. C, CH, and C_2 all react very fast with acetylene (reactions R12–R14). Therefore, the densities of these radicals at the substrate level are below the TIMS detection limit under $F \gg 1$ conditions. Their maximum densities at 55 cm appear at about $F \sim 0.5$ and are equal to $2.8^{+2.5}_{-1.8} \times 10^{17}$, $1.9^{+1.7}_{-1.2} \times 10^{16}$, and $1.1^{+1.0}_{-0.7} \times 10^{17}$ m^{-3} for C, CH, and C_2, respectively.

There is a difference between the C radical and the CH and C_2 radicals. The carbon atom is the "end" radical product of the plasma chemistry under the $F < 1$ conditions, since all other primary products (CH, CH_2, C_2, and C_2H) decompose further in secondary CT and DR reactions, forming C as a reaction product. This shifts the C maximum density (at 25 cm) toward a lower C_2H_2 flow with respect to the CH and C_2 maxima. The same arguments explain also why the C atom has the highest measured density under $F \sim 0.5$ conditions. The model simulation is in agreement with the suggested reaction scheme.

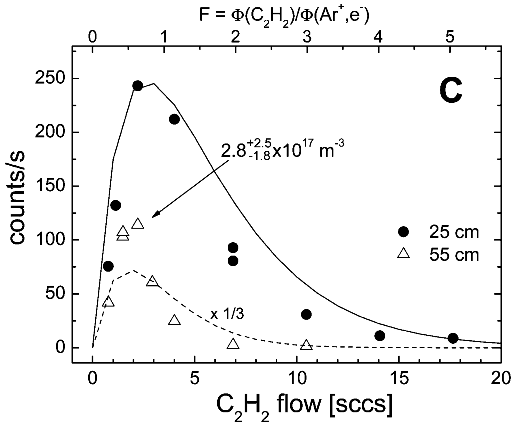

Figure 8. TIMS C radical measurement together with the simulated results (lines).

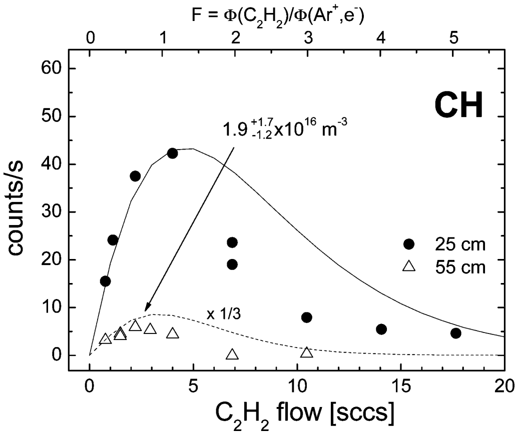

Figure 9. TIMS CH radical measurement together with the simulated results (lines).

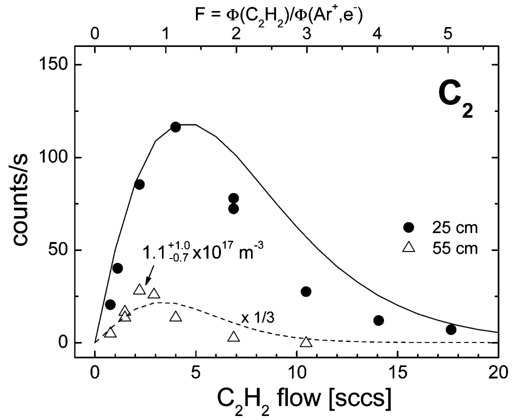

Figure 10. TIMS C_2 radical measurement together with the simulated results (lines).

Discussion. All primary reaction products are formed in the CT and DR reaction steps, and they can be found under $F \leq 1$ conditions, when enough argon ions and electrons are available for these reactions in the ETP. Figure 11 summarizes the reaction scheme under these conditions.

With the knowledge of absolute radical densities, we can now have a closer look at the primary DR reaction R2. The product

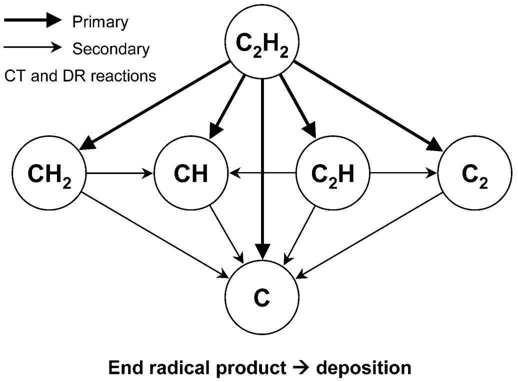

Figure 11. Reaction scheme under $F < 1$ conditions when the CT reactions with argon ion followed by DR with electron dominate the plasma chemistry.

yields of reaction R2 were measured in the ion storage ring experiments.[29] C_2H_2 ions were prepared in a low pressure plasma ion source, stored for 4 s in a heavy-ion storage ring, and cooled with an electron cooler. After the cooling, when the ions were in the $HC{\equiv}CH^+$ geometry, they collided with electrons at a maximal collision energy of 7.4 meV. Neutral products and their relative yields were measured. $C_2H + H$ was found to be the dominant reaction channel (reaction yield 0.50 ± 0.06), followed by $C_2 + H + H$ (0.30 ± 0.05), $CH + CH$ (0.13 ± 0.01), $C + CH_2$ (0.05 ± 0.01), and $C_2 + H_2$ (0.02 ± 0.03). However, when these yields are used in our plasma chemistry simulation model, the relative magnitudes of simulated densities do not correspond with the experimental results. The measured CH density is much lower, and the C and CH_2 densities are higher than those predicted by the simulation model (even when the measured CH_2 density is assumed to be overestimated by a factor of 2). The comparison is made at $F > 1$ where the reactions with C_2H_2 (with reliable reaction rates known from the literature, cf. references in Table 2) are dominant loss processes for all of the radicals.

Using modified product yields of about 0.26, 0.41, 0.07, 0.26, and 0.00 for reactions R2a−R2e, respectively, a reasonable agreement between the simulated and experimental C, CH, CH_2, C_2, and C_2H relative abundances is obtained. The difference between the ion storage ring experiment and ETP conditions lies most probably in the different internal excitation of the C_2H_2 ion formed in the CT process. Due to the lower ionization potential of C_2H_2 (11.4 eV) compared to argon (15.76 eV), additional internal energy is available, which allows the formation of intermediates such as the vinylidene ion ($H_2C{=}C^+$) isomer. The DR of the $H_2C{=}C^+$ ion with electron will preferably yield the $CH_2 + C$ channel and suppress the $CH + CH$ and $C_2H + H$ channels. It could therefore explain the experimental observations. Of course, one should keep in mind that the species densities are calibrated with possible systematic errors (as indicated) and the simulation model is still rather simple. Moreover, some reaction yields as well as the rates of other reactions in Tables 1 and 2 were only estimated. Therefore, the product yields of reaction R2 used in the model should be taken with care. They indicate however that additional internal energy of the molecular ion strongly influences DR reaction yields. No attempt was performed to optimize the reaction yields of reactions R4 and R10.

The experimental results for C, CH, CH_2, C_2, and C_2H radicals at a distance of 55 cm can now be directly compared with the measured growth flux for 48 A, shown in Figure 2. The contribution of the reactive species to the growth is dependent on their sticking probability at the surface, the particle flux toward the surface, and their mass. Moreover, Chantry[34] has discussed that the overall surface reaction probability (β), which includes both the sticking probability (s) and the surface recombination probability (therefore $1 \geq \beta \geq s \geq 0$), has to be taken into account in calculation of the particle flux toward the surface. Then, the growth flux of particle i in terms of carbon atoms/(s m^2) can be expressed as[34,35]

$$G_i = a_i \frac{1}{4} n_i v_i^{\mathrm{av}} \frac{s}{1 - \beta/2} \quad [\text{C atoms/(s m}^2)] \tag{1}$$

where a_i is the number of C atoms in species i (only the C atoms are taken into account, since the mass of hydrogen is small and can be neglected), n_i is the species density near the surface (measured by TIMS), and v_i^{av} is the average thermal velocity [$\sqrt{(8kT/\pi m)}$]. Additional effects such as a convection or temperature gradient near the surface can play an additional role in the case of ETP; however, we use eq 1 as an approximation to calculate the species contribution to the film growth. Since most of the radicals mentioned have a very high sticking probability close to unity, it is assumed that $\beta = s$ for all of them. A substrate temperature of 523 K is used for the calculation of the average thermal velocity, since the gas temperature is very close to the substrate temperature within one mean free path distance from the surface. Taking the substrate temperature may underestimate the growth flux a little bit, because it is a lower limit of a gas temperature near the surface.

The case when $F \sim 0.5$ (C_2H_2 flow of 2 sccs) is discussed first. Due to the abundance of Ar ions and electrons under these conditions, full depletion of acetylene (cf. the C_2H_2 measurement in Figure 12) and its complete decomposition into C, CH, CH_2, C_2, and C_2H radicals in CT and DR reactions occur. The C, CH, C_2, and C_2H radicals will be the major contributors to the film growth. The sticking probability of C and C_2 on pyrolytic graphite was found to be >0.9 at temperatures below 250 °C,[36] and the sticking probability of C_2H was reported to be in the range 0.8−0.9 on a-C:H.[37] Furthermore, the CH sticking probability at the a-C:H surface is also expected to be close to unity. Therefore, a sticking probability of $s = 1$ is used for all of these radicals (except CH_2) and growth fluxes (at 2 sccs of C_2H_2 flow) of 1.3×10^{20}, 8.8×10^{18}, 7.5×10^{20}, and 2.2×10^{19} carbon atoms/(s m^2) are obtained for C, CH, C_2, and C_2H, respectively. CH_2 was not considered, since it has the lowest density among these radicals. The experimental errors are not shown, but they are larger than the errors shown for the radical densities. The additional uncertainty comes from the uncertain-

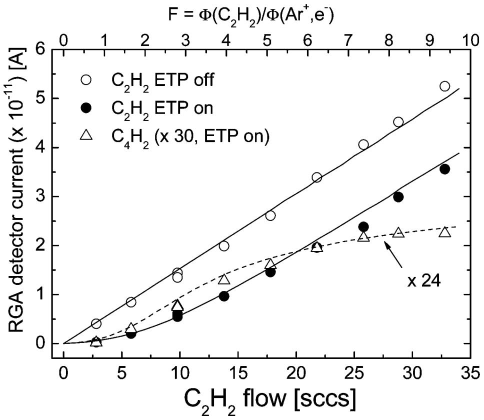

Figure 12. C_2H_2 and C_4H_2 molecules as measured in the plasma background with a residual gas analyzer together with the simulated results (lines).

ties in the sticking and reaction probabilities, the validity of eq 1 (e.g., what is the effect of a temperature gradient close to the surface), and some other gas-sampling issues (the surface temperature is lower than 250 °C during the TIMS measurement, and the sampling orifice is bigger than the particle mean free path, so the radical density is not measured exactly at the substrate plane but slightly above). The C and C_2 radicals have the highest contribution to the growth. When added together, these four species account for 2.5×10^{20} atoms/(s m^2) of the growth flux, which is approximately one-third of the measured total growth flux under these conditions (cf. Figure 2). It seems that the species growth flux is underestimated by a factor of 3, since all possible C_2H_2 dissociation products have been measured. Additionally, the ion contribution to the growth can be neglected, as checked by the simulation model, which indicates that the ion densities are 2 orders of magnitude smaller than the radical densities. The calculated growth fluxes of other radical species presented later in this paper also indicate that their sum is just one-third of the value necessary to explain the growth (cf. the summary in Figure 25 at the end of this article). The fact that this discrepancy is observed through all of the experimental conditions and through all of the radicals indicates that some factor common to all radicals is neglected or, despite our great effort to eliminate all possible systematic errors, some additional systematic error is present in the density determination. For example, the fact that large temperature and density gradients are formed in the flow stagnation region can result in higher growth fluxes than those predicted by eq 1.

Soft and porous polymer-like a-C:H films with a low refractive index (Figure 3), density of 1.2 g/cm^3, hardness of 4 GPa, and hydrogen content higher than 40% are obtained under $F < 1$ conditions. Combining the material properties with TIMS results, it can be concluded that C and C_2 radicals (with a small contribution of CH and C_2H) account for the deposition of soft a-C:H films under $F < 1$ conditions. The film analysis results imply that an additional incorporation of atomic hydrogen has to be taken into account to be able to explain the high hydrogen content in the film.[17] The model predicts an atomic hydrogen density in the gas phase near the substrate approximately 1.3 times higher than the C density, which should in principle supply enough hydrogen atoms to reach the measured hydrogen content of 40% in the film. Molecular dynamic studies have already confirmed that atomic hydrogen can be incorporated into the growing film.[38] At high C_2H_2 flows ($F \gg 1$), the densities of C, CH, CH_2, and C_2 are below the TIMS detection limit and the C_2H density is below 2×10^{16} m^{-3}. Nevertheless, the growth flux (Figure 2) and the refractive index (Figure 3) reach their maximum. These observations exclude primary and secondary products of CT and DR reactions from being dominant growth precursors for hard a-C:H films in the Ar/C_2H_2 ETP.

Secondary Reaction Products. The fastest growth and best mechanical properties of a-C:H films are achieved under the conditions of high C_2H_2 flow ($F \gg 1$). It is therefore important to measure the products of reactions of primary C_2H_2 dissociation products with C_2H_2 (cf. reactions R11−R15 in Table 2).

C_4H_2. Most information is available for reaction R15 of C_2H with C_2H_2 because of its importance in C_2H_2 combustion processes and in planetary atmospheric environments.[39,40] The reaction rate is temperature independent, and the only exothermic channel is the production of the C_4H_2 molecule (1,3-butadiyne) and atomic hydrogen.[41] C_4H_2 was detected in the ETP background previously by means of a residual gas analyzer (RGA, K. J. Lesker AccuQuad 200D) mounted on the sidewall of the reactor in the separate, differentially pumped chamber connected to the main vessel by a 100 μm orifice.[17] These measurements are shown together with the measurement of C_2H_2 under plasma off and on conditions in Figure 12. The C_2H_2 flow was extended in this case up to 34 sccs in order to see whether the C_4H_2 signal saturates at high C_2H_2 flows. The TIMS measurement of C_4H_2, shown elsewhere,[42] corroborates the RGA results. Moreover, the C_4H_2 density can be calibrated. At an arc current of 48 A and a C_2H_2 flow of 18 sccs, the C_4H_2 density equals $5.6^{+4.9}_{-3.5} \times 10^{19}$ m^{-3} (CO_2 gas was used in the C_4H_2 calibration procedure).

The C_4H_2 has clear second-order behavior. It is not present in ETP at $F < 1$, because there is not enough C_2H_2 available for secondary reactions. At very high C_2H_2 flows, the C_4H_2 density saturates because the C_4H_2 production is limited by the amount of available Ar^+ and e^- for the C_2H production in CT and DR reactions R1 and R2a. Both C_2H_2 and C_4H_2 RGA measurements can be well simulated by the plasma chemistry model results at 55 cm. C_4H_2 is the stable molecule, and its abundant presence in the background is evidence that it has negligible reaction probability at the a-C:H surface and that it does not contribute to the deposition.

C_4 and C_4H. Figures 13 and 14 show measurements of the C_4 and C_4H radicals. Their behavior has second-order character similar to the C_4H_2 molecule. Moreover, both C_4 and C_4H react with C_2H_2, since their relative densities decrease with increasing acetylene flow. The loss process is also clearly visible when the 25 and 55 cm measurements are compared. Only C_2 and C_2H from primary products can form in reaction with C_2H_2, a species with four carbon atoms. Recently, it was shown that the C_4H radical is also produced in a slightly endothermic reaction (R15b),[41] but it is a minor branch of reaction R15 and

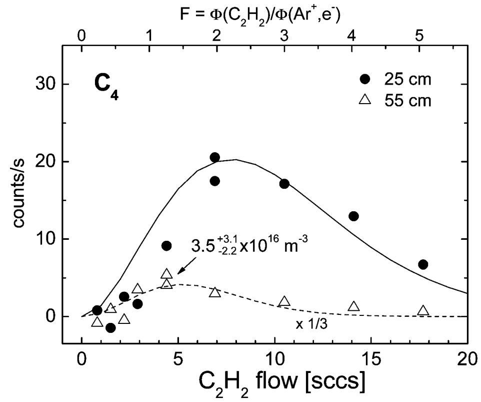

Figure 13. TIMS C_4 radical measurement together with the simulated results (lines).

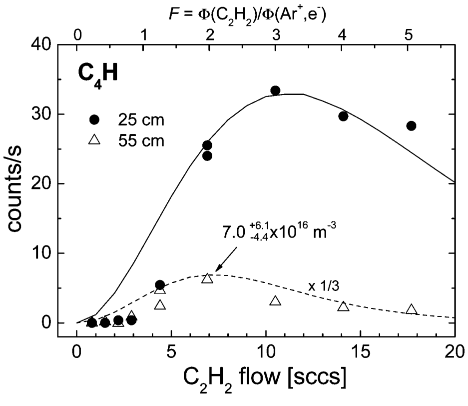

Figure 14. TIMS C_4H radical measurement together with the simulated results (lines).

is neglected in the simulation model. Kaiser et al.[43] studied experimentally reaction R14 of the C_2 radical with C_2H_2. They observed that when the collision energy of the reactants is smaller than 0.25 eV, the C_4H radical is the only product of reaction R14, contrary to the fact that the C_4 branch (R14b) is also exothermic. Since the C_4 radical is measured in the plasma, it is expected that the internal excitation of the C_2H radical opens up the C_4 production channel (reaction R14b). A reaction yield of 0.5 was used in the simulation model for both the R14a and R14b channels without any optimization. Another possible channel producing C_4 and C_4H radicals is the CT reaction of C_4H_2 with an Ar ion followed by the DR of a C_4H_2 ion with an electron.[44] The significance of these reactions was tested in the simulation model, with a rather high CT reaction rate of 6×10^{-10} cm^3/s and a DR rate of 3×10^{-7} cm^3/s, but it had a marginal influence ($<5\%$) on the final plasma composition.

There are some differences between C_4 and C_4H. The C_4H measurement at 25 cm has a longer “tail” (higher signal) than the C_4 radical at high C_2H_2 flows. Furthermore, the maximum C_4H density at 55 cm (equal to $7.0^{+6.1}_{-4.4} \times 10^{16}$ m^{-3}) is measured at a C_2H_2 flow of 7 sccs, whereas the maximum for the C_4 radical ($3.5^{+3.1}_{-2.2} \times 10^{16}$ m^{-3}) lies between 4 and 5 sccs. This difference can be subscribed to the smaller reaction rate of the C_4H radical with C_2H_2 in comparison with C_4. To our knowledge, no experimental or theoretical data on these reaction rates are available, but a similar difference is observed also for C_2 and C_2H radicals. The reaction rates k_{20} and k_{21} were selected in such a way that simulated densities fitted the experimental data reasonably well.

The maximum C_4 and C_4H growth fluxes 5.8×10^{18} and 2.1×10^{19} carbon atoms/(s m^2) (under a C_2H_2 flow of 18 sccs, using a sticking probability of 1) are more than 20 times lower than the measured growth flux 1.7×10^{21} carbon atoms/(s m^2), again indicating that these radicals are not the major contributors to the film growth. However, their incorporation into the films is highly probable and they can be responsible for a higher carbon content in the films deposited under moderate C_2H_2 flow conditions in the range from 4 to 6 sccs as observed by Rutherford backscattering spectroscopy/elastic recoil detection analysis measurements.[17]

C_3H_2, C_3H, and C_3. The C_3, C_3H, and C_3H_2 radicals turned out to be the species with an unexpected behavior. They were successfully detected with ionization potentials (IPs) of 12.1 ± 0.2, 9.7 ± 0.2, and 9.2 ± 0.2 eV, respectively.[25] The density measurements at 25 cm at an arc current of 48 A and at 55 cm at arc currents of 22, 48, and 61 A are shown in Figures 15−17. C_3, C_3H, and C_3H_2 are expected to be formed in reactions of C and CH with C_2H_2. The branches of the C_2 reaction with C_2H_2 (R14d−f) are more than 1 eV endothermic (cf. Table 2) and can probably be excluded. There is a clear difference between the behavior of the C_3 and C_3H radicals and the C_3H_2 radical as a function of the C_2H_2 flow. Both C_3 and C_3H have second-order behavior with the production limited by the available amount of argon ions and electrons (C_3 and C_3H density saturates at $F \gg 1$, where the argon ions and electrons are fully depleted) and without any significant loss process in the gas phase. Indeed, the reaction rate of C_3 with C_2H_2 was measured up to a temperature of 610 K[45] and it was found to be in the order of 10^{-14} cm^3 s^{-1}. Such a small reaction rate results in a lifetime of the C_3 radical in the ETP in the order of seconds. (C_3 lifetime is estimated as $1/(n_{C_2H_2}k_{C_2H_2+C_3})$ which gives at a density of 10^{14} cm^{-3} C_2H_2 a value of 1 s.) The reaction rate of C_3H with C_2H_2 is expected to be in the same order, since both are resonantly stabilized radicals, where the unpaired electrons are delocalized as a result of two or more existing resonant electronic structures. It should be noted that two isomeric forms, cyclic and linear, are allowed for both C_3[46] and C_3H,[47] but it was not possible to distinguish which isomeric forms were detected. The maximum densities of C_3 and C_3H at a C_2H_2 flow of 18 sccs and at a distance of 55 cm and arc current of 48 A were determined to be $5.8^{+5.1}_{-3.6} \times 10^{17}$ and $1.2^{+1.1}_{-0.8} \times 10^{17}$ m^{-3}. The C_3 radical has the highest density of all measured radicals under 48 A and $F > 1$ conditions.

The C_3H_2 radical was identified as cyclopropenylidene, the most stable C_3H_2 structure,[25,48,49] and its measurement is shown in Figure 17. Its density does not saturate when $F \gg 1$, and it

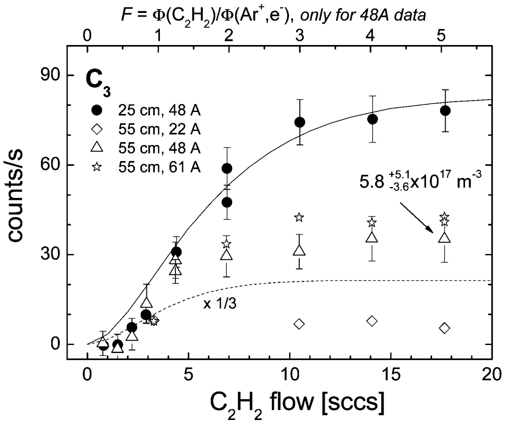

Figure 15. TIMS C_3 radical measurement at arc currents of 22, 48, and 61 A together with the simulated results for measurements at 48 A (lines).

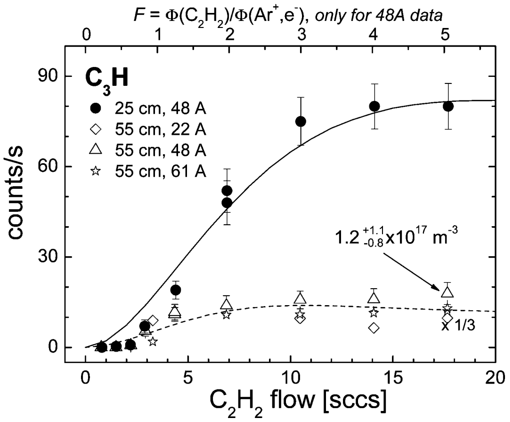

Figure 16. TIMS C_3H radical measurement at arc currents of 22, 48, and 61 A together with the simulated results for measurements at 48 A (lines).

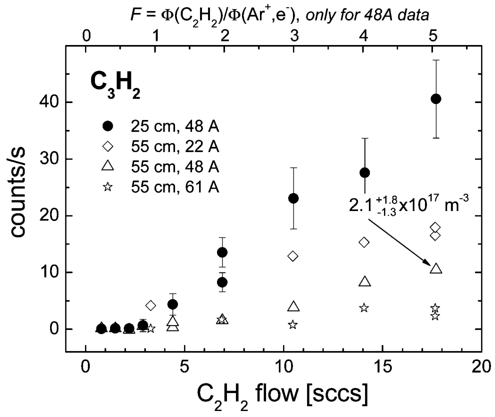

Figure 17. TIMS C_3H_2 radical measurement.

also decreases with increasing arc current, which means that its production is not limited by the available amount of argon ions and electrons. The C_3H_2 measurement is similar to the results for the CH_3, CH_4, C_3H_4, C_5H_4, and C_6H_6 species (shown later in Figure 22), which all scale approximately with the amount of unconsumed C_2H_2 (cf. Figure 12). It leads us to the conclusion that the C_3H_2 radical is not produced in the forward ETP chemistry but is a product of some background process involving C_2H_2. One possibility could be a C_2H_2 pyrolysis on the cascaded arc nozzle. The nozzle serves as an anode in the cascaded arc electric circuit; it collects electrons and gets heated, especially when an insulating a-C:H layer is deposited on it (cf. illustration in Figure 4). Under $F > 1$ conditions, a sootlike deposition around the nozzle exit is observed, which glows during the plasma operation, and C_2H_2 pyrolysis occurs most probably at this place. The C_3H_2 formation in pyrolysis on the arc nozzle, at the upper part of the reactor, is consistent with the observed C_3H_2 density drop between 25 and 55 cm.

The fact that C_3H_2 is not produced in the ETP chemistry is a surprising result. Reaction R12 of the CH radical with C_2H_2, in which C_3H_2 can be produced, was studied both theoretically and experimentally. Boullart et al.[49] detected the C_3H_2 (identified as cyclopropenylidene cyc-C_3H_2) by means of TIMS in $C_2H_2/O_2/H_2$ flames and derived the product yield of reaction R12 to be 85^{+9}_{-19}% C_3H_2 plus H and 15^{+19}_{-9}% C_3H plus H_2. A theoretical calculation by Vereecken et al.[50] found prop-2-ynylidene (HCCCH) plus H to be a dominant exit channel (80−90%, pressure <10 atm), followed by cyclopropenylidene plus H (∼10%) and propynilidine (lin-C_3H) plus H_2 (2−5%). The production of C_3 plus H_2 and H in this reaction was not observed because it is more than 2 eV endothermic (using the enthalpies listed in ref 31). It seems that C_3H_2 formation in reaction R12 is suppressed under Ar/C_2H_2 ETP conditions and the channel in which molecular hydrogen is expelled from the C_3H_3 complex formed in the CH + C_2H_2 reaction is favored. This behavior is most probably caused by the internal energy of the CH radical, which can be relatively large, since it was formed from a superexcited C_2H_2 complex with an internal energy of up to 15.76 eV, reaction R2c. The additional internal energy can critically influence the dissociation of the C_3H_3 complex and leads to preferential $C_3H + H_2$ formation. Only channel R12b with a product yield equal to 1 is used in the model for reaction R12.

The C_3 radical is produced dominantly in reaction R11 of C with C_2H_2. This reaction has two exothermic channels: C_3H + H and $C_3 + H_2$. The product yields were studied by the crossed molecular beam technique for C(^3P_J, $^1D_2$) reaction with C_2H_2,[51] and it was found that both C_3H and C_3 species are produced with similar yields. As a consequence, the C_3H density should be higher than the C_3 density, since it is also formed in reaction R12. However, the measured C_3 density is significantly higher than the C_3H density, which is evidence that reaction R11 yields preferably $C_3 + H_2$ under Ar/C_2H_2 ETP conditions, again favoring the expulsion of the molecular hydrogen from the C_3H_2 reaction complex. As in the case of reaction R12, we can argue that this behavior is a result of the additional internal excitation energy of the C_3H_2 complex. It was shown that the C atom is produced in a highly excited state[16] combined additionally with a 1500 K gas (C_2H_2) temperature in the ETP under 48 A arc current conditions. Only the $C_3 + H_2$ channel of reaction R11 is taken into account in the simulation model.

A difference is observed between C_3 and C_3H. The C_3 density drops less than the density of the C_3H radical between distances of 25 and 55 cm, which implicates that there is another production channel for the C_3 radicals but not for the C_3H radicals. Another remarkable fact is that the C_3H density at 55 cm shows only a small variation as a function of the arc current compared to the C_3 density, which increases with increasing arc current. We suggest that the H-shifting reaction

$$C_3H + H \leftrightarrow C_3 + H_2 \quad (\Delta H_r = -0.36\ \text{eV}) \qquad (R22)$$

is a possible source of additional C_3 in Ar/C_2H_2 ET and it can also account for C_3H density behavior with respect to the arc current. Hydrogen atoms will be abundantly present in the expanding beam, since they are formed in most of the hydrocarbon reactions. Furthermore, their reactivity with C_2H_2 is very small.[52] Since the increase of the C_3 density is experimentally observed, we incorporated only the forward reaction R22 in the model with an estimated reaction rate of 2×10^{-10} cm^3 s^{-1}. The backward reaction would require the knowledge of the reaction equilibrium constant and the H_2 density. The importance of H-shifting reactions in a dc-arc jet CH_4/H_2 CVD reactor was shown by Mankelevich et al.[53] In the same paper, they also presented results of simulation of Ar/C_2H_2 ETP chemistry and predicted that the C_3 radical is (together with C_3H) one of the dominant radical products with a density of 7×10^{17} m^{-3}, in good agreement with the TIMS measured density.

Discussion. The most important question is whether C_3, C_3H, and C_3H_2 radicals are significant contributors to the a-C:H film growth. The C_3H_2 radical can be ruled out immediately on the basis of the fact that its density increases with increasing C_2H_2 flow (without any saturation) and decreases with increasing arc current, with both trends going opposite to the one observed for the growth flux (Figure 2). The C_3H_2 density at 48 A and a C_2H_2 flow of 18 sccs equals $2.1^{+1.8}_{-1.3} \times 10^{17}$ m^{-3}, which is high enough for a measurable contribution to the film growth, which indicates that the C_3H_2 (cyclopropenylidene) sticking probability at the a-C:H surface is rather low. The C_3H relative density resembles the measured growth flux at C_2H_2 flows higher than 5 sccs (arc current 48 A), but the fact that its density does not increase with increasing arc current and that it is 5 times smaller than the C_3 density favors the C_3 radical to be the probable significant contributor to the growth. The C_3 density shows a trend that corresponds (under $F > 1.5$ conditions) to the growth flux, as is seen in Figure 18, where the TIMS signal for C_3 is plotted against the growth flux. Even better correlation is found between the C_3 count rate and film refractive index plotted in Figure 19. The refractive index is around 1.8 when C_3 is not present in the plasma and is above 2 and linearly increases with increasing C_3 density when the

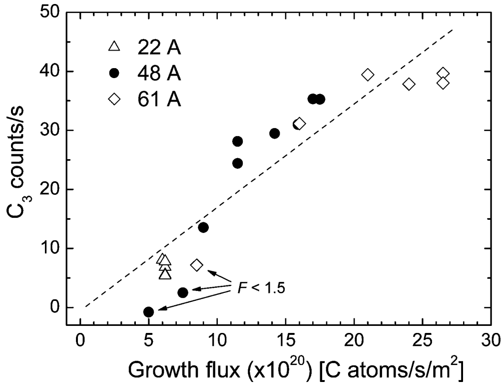

Figure 18. TIMS C_3 radical count rate plotted against the total growth flux.

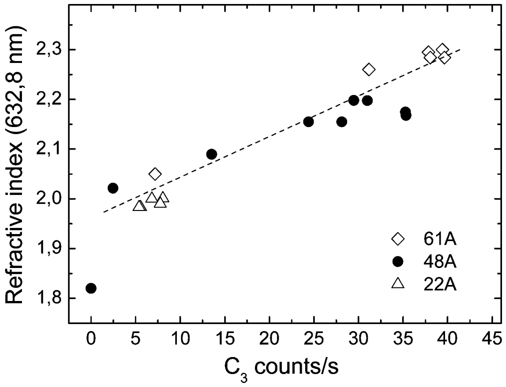

Figure 19. Film refractive index plotted against the TIMS C_3 radical count rate.

C_3 radical is measured by TIMS, which indicates that it is responsible for the film quality in terms of hardness and density. The C_3 radical also has a relatively high sticking probability. It was measured on pyrolytic graphite[36] and was found to be close to unity at room temperature, 0.8 at 250 °C and further decreasing with increasing substrate temperature. Using a sticking probability of 0.8, a C_3 growth flux of 3.3×10^{20} carbon atoms/(s m^2) is obtained (18 sccs of C_2H_2, 48 A arc current), which is the highest growth flux from all species measured and accounts for 19% of the measured a-C:H growth of 1.7×10^{21} carbon atoms/(s m^2). The C_3H growth flux under the same conditions, calculated with the same sticking probability of 0.8, is 6.6×10^{19}, and together with the C_3 radical and the C_5 and C_5H radicals shown later, they account for 32% of the a-C:H growth flux. As in the case of C, CH, C_2, and C_2H radicals, it seems that the growth fluxes of these species are underestimated by a factor of 3. If this is the case, the C_3 radical would be the dominant growth precursor under $F > 1$ conditions. Moreover, the temperature-dependent sticking probability of C_3 can explain the observed decrease of deposition rate at elevated substrate temperatures.[18] However, since the C_3 radical has the highest density and highest growth flux among all of the other radicals measured, and its density is correlated with growth rate and film refractive index, we can certainly conclude that C_3 is a significant contributor to the a-C:H film growth for ETP-CVD.

Diamondlike a-C:H films with a hardness of 14 GPa and a hydrogen content of about 33% are deposited under these conditions. As mentioned in the previous discussion for $F < 1$ conditions, also under $F > 1$ conditions, an additional incorporation of hydrogen in the growing film must occur to explain the film stoichiometry. The model predicts that the atomic hydrogen density close to the surface is approximately twice as high as the C_3 density, which should in principle supply enough hydrogen atoms to reach the measured hydrogen content of 33% in the film. Molecular dynamic studies have already confirmed that atomic hydrogen can be incorporated into the growing film.[38]

Other Detected Species. Next to the primary reaction products and the products of their reactions with acetylene, other radicals such as CH_3, C_5, and C_5H and stable molecules such as CH_4, C_3H_4, C_5H_4, C_5H_6, C_6H_2, and C_6H_6 were detected.

C_5 and C_5H. The C_5 and C_5H radicals were measured with ionization potentials of 11.4 ± 0.5 and 9.8 ± 0.2 eV, respectively, and their relative densities measured at 25 and 55 cm are shown in Figures 20 and 21. These radicals are most probably formed in reactions of C and CH with C_4H_2, reactions R16 and R17, similar to C_3 and C_3H formation in reactions R11 and R12. The comparison of the results at 25 and 55 cm suggests that the reactivity of C_5 and C_5H with C_2H_2 is low, again in analogy with C_3 and C_3H radicals. This similarity is used to estimate the reaction yields and reaction rates for the plasma chemistry simulation model. As can be seen in Figure 20, the C_5 density at a 55 cm distance is slightly bigger than the prediction from the simulation model. It is probable that also C_5 and C_5H radicals are interchanged in the reaction $C_5H + H \leftrightarrow C_5 + H_2$. However, this reaction is not included in the model. The maximum at 55 cm for C_5 and C_5H densities corresponds to $1.3^{+1.1}_{-0.8} \times 10^{17}$ and $7.6^{+6.7}_{-4.8} \times 10^{16}$ m^{-3}, respectively. Assuming a sticking probability equal to the C_3 sticking probability (0.8), the highest possible contribution of these species to the growth flux under a C_2H_2 flow of 18 sccs and an arc current of 48 A can be estimated. The obtained values are 9.3×10^{19} and 5.4×10^{19} carbon atoms/(s m^2), which is more than 3 times lower than the estimated C_3 growth flux.

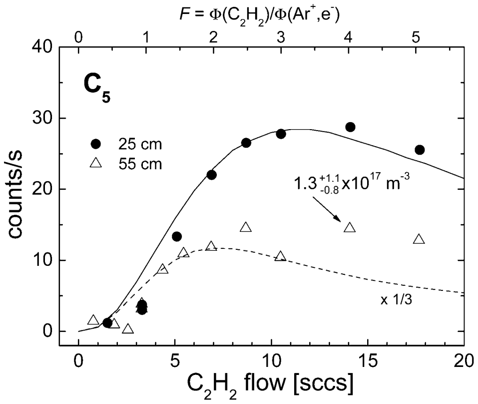

Figure 20. TIMS C_5 radical measurement together with the simulated results (lines).

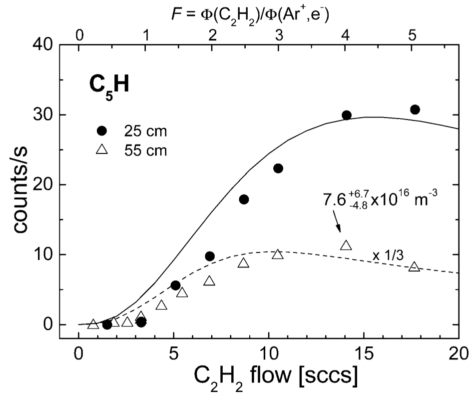

Figure 21. TIMS C_5H radical measurement together with the simulated results (lines).

CH_3, CH_4, C_3H_4, C_5H_4, and C_5H_6. Next to the above-discussed radicals, CH_3, CH_4, C_3H_4, C_5H_4, and C_5H_6 species were also detected (Figure 22). They are not incorporated into the plasma chemistry model. All of them, except C_5H_6, follow the trend similar to C_3H_2, which scales approximately with the amount of unconsumed C_2H_2 that is left after the main plasma chemistry has taken place in the beam. As was already suggested for the C_3H_2 radical, these species are probably formed in the pyrolysis of C_2H_2 on the heated cascaded arc nozzle. The C_5H_6 density scales approximately with the square of the unconsumed C_2H_2, suggesting that it originates in the reaction of one of the species formed in the C_2H_2 pyrolysis with C_2H_2.

The densities of the species in Figure 22 are estimated to be in the range $(0.5-30) \times 10^{17}$ m^{-3} (at an arc current of 48 A and a C_2H_2 flow of 18 sccs), and the most abundant species are C_3H_4 and CH_4 molecules. The fact that the plasma composition

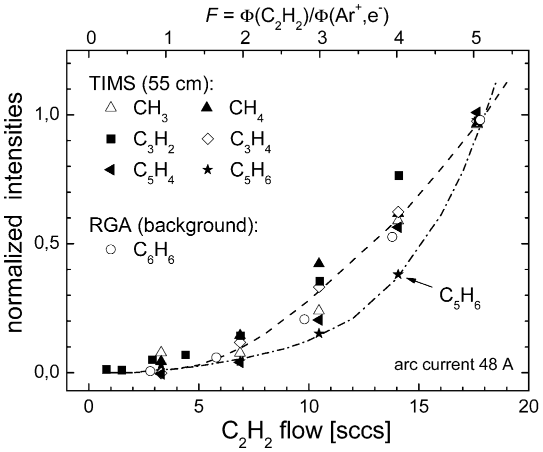

Figure 22. TIMS CH_3, CH_4, C_3H_2, C_3H_4, C_5H_4, and C_5H_6 measurement together with RGA results for C_6H_6. Lines are drawn to guide the eye.

can be successfully modeled without these species and that they are all stable molecules (except CH_3, but it is known that CH_3 surface reaction probability is very small[54]) confirms that they are only background species unaffecting the main plasma chemistry and that they can be neglected when the deposition mechanism is treated.

C_6H_2 and C_6H_6. These stable products were previously measured by the RGA[17] (shown also in Figure 1) at an extended C_2H_2 flow range of 33 sccs and at an arc current of 48 A (Figure 23). The C_6H_2 and C_6H_6 densities were not calibrated with TIMS, but from the comparison of the RGA signal intensity, it can be estimated that $n_{C_5H_{y,y=4,6}} < n_{C_6H_6} < n_{C_6H_2} < n_{C_4H_2}$ under all of the conditions measured. C_6H_2 can be formed in a reaction of C_2H with C_4H_2 (R19) and C_4H with C_2H_2 (R20). The results from the simulation model for C_6H_2 are also shown in Figure 23. Since C_6H_2 is a relatively stable molecule, its contribution to the a-C:H growth is considered to be negligible.

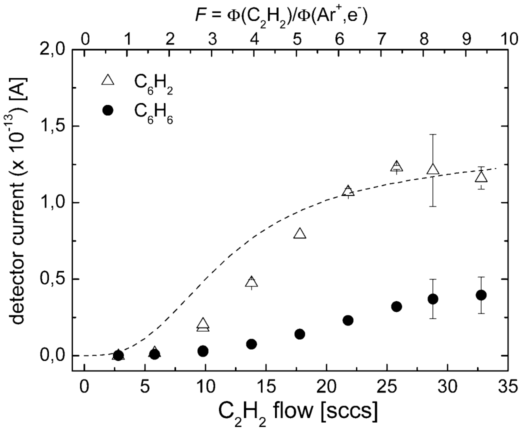

Figure 23. C_6H_2 and C_6H_6 molecules as measured in the plasma background with a residual gas analyzer together with the simulated results for a C_6H_2 molecule.

The C_6H_6 molecule has similar behavior to the CH_3, CH_4, C_3H_2, C_3H_4, C_5H_4, and C_5H_6 species, and its density measurement is also shown in Figure 22. It was not resolved which of many possible C_6H_6 isomers[55] was detected. However, the role of C_6H_6 in the plasma chemistry and deposition can also be neglected.

5. Conclusions

The plasma chemistry occurring in an Ar/C_2H_2 ETP has been characterized in detail by means of TIMS. The C_2H_2 dissociation is initiated in a CT reaction between an argon ion and the C_2H_2 molecule followed by a DR of internally excited $C_2H_2^+$ with an electron. C, CH, CH_2, C_2, and C_2H, primary reaction products, are formed in this CT and DR step. Our results strongly suggest that branching ratios of the DR of the formed $C_2H_2^+$ ion are different from the reported values measured in storage ring experiments for the ground state $C_2H_2^+$ ion.[29] Due to the difference between the ionization potentials of argon and C_2H_2, the formed $C_2H_2^+$ possesses additional internal energy of up to $15.76 - 11.40 = 4.36$ eV. The internal excitation allows $C_2H_2^+$ rearrangement into intermediates such as the $H_2C{=}C^+$ isomer. When these intermediates recombine with electrons, they dissociate likely to $CH_2 + C$ products and the $CH + CH$ and $C_2H + H$ channels are, compared to the DR of the $HC{\equiv}CH^+$ ion, suppressed.

The plasma chemistry and the following plasma composition are determined by the initial ratio F between the C_2H_2 flow through the injection ring and the argon ion and electron fluence from the plasma source. The CT and DR reactions dominate the plasma chemistry under $F < 1$ conditions, and the products of primary C_2H_2 dissociation products are decomposed even further. The main plasma chemistry end products are then carbon atoms, as depicted schematically in the plasma chemistry scheme in Figure 11.

On the other hand, when the C_2H_2 flow is higher than argon ion and electron fluence ($F > 1$), the most important reactions are those involving C_2H_2 and primary radicals. Two branches are identified in the plasma chemistry under these conditions, depending on whether an even or odd number of carbon atoms is involved in the reactions. The reaction of $C_{2n}H$ radicals with C_2H_2 leads to the formation of stable $C_{2(n+1)}H_2$ molecules, whereas the reaction of carbon clusters C_{2n} with C_2H_2 forms $C_{2(n+1)}H_{y(y=0,1)}$ radicals, which are further reactive with C_2H_2 and other stable molecules, as illustrated on the right-hand side of the reaction scheme presented in Figure 24. The plasma chemistry can propagate toward larger hydrocarbon molecules through these polymerization reactions. Stable hydrocarbon molecules with an even number of carbon atoms ($C_{2n}H_2$), which are commonly measured in C_2H_2 plasmas, are formed in this branch. On the contrary, the C and CH radicals react with C_2H_2 (C_4H_2) and form C_3 and C_3H (C_5 and C_5H) radicals which, due to their resonant stabilization, are unreactive in the gas phase with stable molecules and are, in this sense, the plasma chemistry end products (cf. the left-hand side of Figure 24).

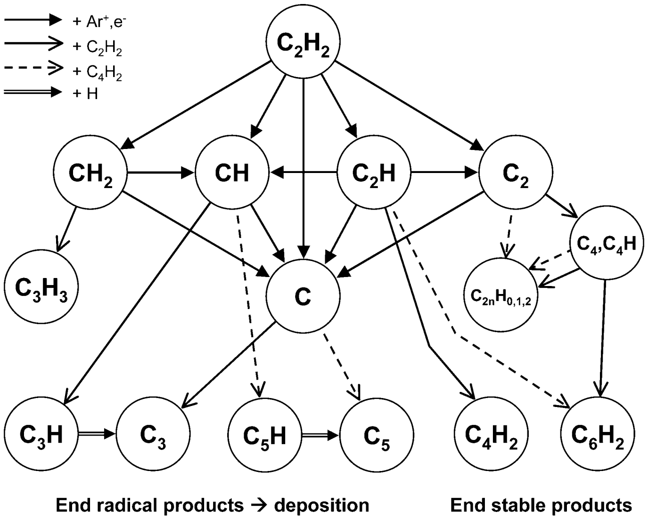

Figure 24. Reaction scheme of Ar/C_2H_2 ETP chemistry.

Furthermore, the gas temperature 1500 K and the internal excitation of the C and CH radicals create conditions under which the formation of $C_3 + H_2$ and $C_3H + H_2$ from C_3H_2 and C_3H_3 reaction complexes, respectively, is favored over other possible reaction channels.

Moreover, the H-shifting reaction of atomic hydrogen with C_3H (C_5H) leads most probably to additional C_3 (C_5) formation. Radical−radical reactions can be neglected under the Ar/C_2H_2 ETP conditions due to relatively small radical densities compared to stable molecules or argon ions and electrons densities and due to the short reaction time in the ETP beam. The products of C_2H_2 (and probably also C_4H_2 and C_6H_2) background chemistry, most probably pyrolysis on the hot arc nozzle, were detected next to the forward ETP plasma chemistry products. However, their influence on the plasma composition and the growth is found to be negligible.

The growth fluxes of the species with the highest contribution to the growth are plotted in Figure 25 together with the total measured growth flux from Figure 2. It can be seen that when all of the contributions are added, the shape of the measured growth flux with respect to the C_2H_2 flow can be reasonably reproduced. However, the sum of the calculated growth fluxes accounts, through all the conditions measured, for approximately only 30% of the measured growth flux (note the different scales of the left and right axes in Figure 25). The fact that this discrepancy is observed through all of the experimental conditions and through all of the radicals indicates that some factor common to all radicals is neglected (e.g., the large temperature and density gradients formed in the flow stagnation region can result in higher growth fluxes than those predicted by eq 1) or, despite our great effort to eliminate all possible systematic errors, some additional systematic error is present in the density determination [e.g., some additional effects resulting from the differences between plasma on conditions (radical measurements) and plasma off conditions (calibration gas measurement)]. There is also the possibility of contribution of some additional species to the growth, but we find it less probable, since all possible dissociation products of C_2H_2 were measured under the $F < 1$ conditions and still these species account only for 30% of the growth flux. Anyhow, the C_3 density and the C_3 growth flux are the highest among all radical densities and growth fluxes and we identify the C_3 radical as a significant growth precursor of Ar/C_2H_2 deposited a-C:H film.

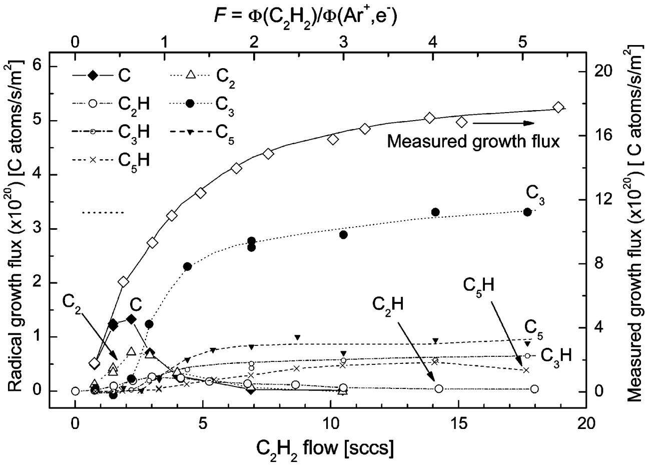

Figure 25. Comparison of the growth fluxes, calculated from the TIMS density measurements, to the measured total growth flux. Note the different scales of the left and right axes.

The deposited a-C:H films reflect the plasma composition close to the substrate plane. Under $F < 1$ conditions, the flux toward the surface is dominated by C and C_2 radicals (with an additional small contribution of CH and C_2H radicals). The deposited films are porous, soft, and polymer-like with a roughness of about 8 nm.[17] The hydrogen content is larger than 40%, which implies that an additional flux of hydrogen atoms is needed to explain the film C:H stoichiometry.

a-C:H films with a hardness of 14 GPa and a hydrogen content of 33% are deposited under $F > 1$ conditions. Radicals with an odd number of carbon atoms, the C_3, C_3H, C_5, and C_5H radicals, are responsible for the growth because they are unreactive with C_2H_2 (and other stable hydrocarbons) in the gas phase. The contribution of the radicals with an even number of carbon atoms is small, because they are reactive in the gas phase. The C_3 radical has the highest density and is identified as a significant, and also probably dominant, growth precursor of hard a-C:H films. The growth rate as well as film quality in terms of refractive index are correlated to the density of this radical. Again, as in the $F < 1$ case, the relatively high H content in the film requires an additional hydrogen flux toward the surface. Atomic hydrogen coming from the plasma is most probably incorporated in the film. Feasibility of atomic hydrogen incorporation in the growing film was confirmed by molecular dynamic calculations,[38] and the plasma chemistry simulation model predicts that its density in the plasma is sufficient.

Acknowledgment. The authors thank S. Agarwal (University of Massachusetts at Amherst) and W. M. M. Kessels for fruitful discussions about the TIMS design and measurements, K. G. Y. Letourneur for the initial help with the plasma chemistry simulation model, A. Von Keudell (Ruhr University, Bochum) for fruitful discussions about the possible a-C:H growth mechanism, E. Neyts and A. Bogaerts (University of Antwerp) for molecular dynamic simulation of a-C:H growth, and M. J. F. van de Sande, J. F. C. Jansen, A. B. M. Hüsken, and H. M. M. de Jong for their skillful technical assistance. This work is part of the research program of the "Stichting voor Fundamenteel Onderzoek der Materie" (FOM). Additional funding was received from NATO Science for Peace Project No. 974354.

Appendix: Plasma Chemistry Simulation Model

Here, the description of the plasma chemistry simulation model is given. The simulation model solves the conservation equations for the species densities given by

$$\frac{\mathrm{d}n_i(\vec{r},t)}{\mathrm{d}t} = \frac{\partial n_i}{\partial t} + \nabla(n_i\vec{u}) = \left[\frac{\partial n_i}{\partial t}\right]_{\mathrm{coll}} \qquad (A.1)$$

The right-hand side describes the particle production and elimination in the collisions with other species. The radiation processes are neglected here. The plug-down geometry of the ETP allows the transformation of the problem into a quasi-one-dimensional situation, assuming that the species density is homogeneous across the expanding beam and the beam divergence is described by a z-dependent beam cross-sectional area $A(z)$,[56]

$$\frac{1}{A(z)}\frac{\partial}{\partial z}(A(z)\cdot n(z)\cdot u(z)) = \left[\frac{\partial n_i}{\partial t}\right]_{\mathrm{coll}} \qquad (A.2)$$

where u is the drift or directed velocity. Steady state plasma conditions were assumed. When u is in a first approximation assumed constant, eq A.2 can be rearranged into

$$u\frac{\partial}{\partial z}n(z) = -u\cdot n(z)\frac{1}{A(z)}\frac{\partial}{\partial z}A(z) + \left[\frac{\partial n_i}{\partial t}\right]_{\text{coll}} \qquad \text{(A.3)}$$

The main collision production and loss processes are the chemical reactions and CT and DR reactions. Collision processes requiring significant threshold energy, such as electron impact dissociation or ionization, can be neglected due to the low electron temperature (<0.3 eV). The last term of eq A.3 can be written as

$$\left[\frac{\partial n_i}{\partial t}\right]_{\text{coll}} = \sum_{l,m} \pm k_{lm} n_l n_m \qquad \text{(A.4)}$$

where k_{lm} is the reaction rate between species l and m and the summation is performed over all reactions in which species i is a product (+) or a reactant (−). The divergence of the plasma beam in the subsonic part is determined by radial diffusion. As an approximation, the angle φ between the plasma boundary and the plasma axis at each axial position can be expressed by[33]

$$\tan\varphi = F_{\text{p}}\frac{D_{12}}{u\cdot r_{\text{p}}(z)} \quad \left(= \frac{\mathrm{d}r_{\text{p}}(z)}{\mathrm{d}z}\right) \qquad \text{(A.5)}$$

where D_{12} represents the binary diffusion coefficient and $r_{\text{p}}(z)$ the plasma radius at axial position z (cf. Figure 4). The coefficient F_{p} depends on the actual radial profile of the particle densities in the plasma beam. However, a number of common profiles (Gauss, Lorentz, Bessel, parabola) yield approximately the same result ($F_{\text{p}} = 2 \pm 20\%$).[33] D_{12} can be approximated by

$$D_{12} = \frac{3}{8N_{\text{A}}\sqrt{2\pi}}\frac{(RT)^{3/2}}{pd_{12}^{\,2}}\sqrt{\frac{1}{M_1} + \frac{1}{M_2}} \qquad \text{(A.6)}$$

where N_{A} is Avogadro's number, R the universal gas constant, p the pressure in pascals, T the gas temperature in kelvins, d_{12} the averaged hard sphere radius, and $M_{1,2}$ the molar masses of colliding particles. The main colliding partner is the argon atom, since the plasma beam dominantly consists of them. As an approximation, we used the same collision cross section of 1×10^{-19} m^2 for all of the species. By solving differential equation A.5 for the beam radius, we obtain

$$r_{\text{p}}(z) = \sqrt{r_0^{\,2} + 2\frac{FD_{12}}{u}z} \qquad \text{(A.7)}$$

where r_0 is the beam radius at $z = 0$. The plasma beam area cross section can now be expressed and substituted into eq A.3. The continuum equation describing the particle density along the expansion axis is finally

$$u\frac{\partial}{\partial z}n(z) = -\left(\frac{r_0^{\,2}}{2FD_{12}} + \frac{z}{u}\right)^{-1} n(z) + \sum_{l,m} \pm k_{lm} n_l n_m \qquad \text{(A.8)}$$

The set of differential equations was solved using a Fehlberg fourth−fifth-order Runge−Kutta method (Maple 6 program) assuming $u = 1000$ m/s, $p = 29$ Pa, and $T = 1500$ K (gas temperature derived from the Doppler broadening of the carbon absorption line and C_2 and CH rotational spectra). The initial C_2H_2 density at $z = 0$ is calculated from the C_2H_2 flow in standard cubic centimeters per second:

$$n_{C_2H_2}(z=0) = \frac{F_{C_2H_2}\cdot 2.69 \times 10^{19}[\text{s}^{-1}]}{1000[\text{m s}^{-1}]\cdot\pi\cdot 0.045^2[\text{m}^2]}[\text{m}^{-3}] \qquad \text{(A.9)}$$

The C_2H_2 flow is a model parameter and is varied from 0 to 34 sccs in steps of 1 sccs in order to get number densities at the given distance as a function of acetylene flow. The initial argon ion and electron density (equal to each other) and initial ETP beam radius (r_0) were used as fitting parameters in order to obtain the best agreement between measured and simulated data.

References and Notes

(1) Aisenberg, S.; Chabot, R. *J. Appl. Phys.* **1971**, *42*, 2953.

(2) Robertson, J. *Mater. Sci. Eng.* **2002**, *R37*, 129.

(3) Novikov, N. V.; Gontar, A. G.; Khandozhko, S. I.; Kutsay, A. M.; Tkach, V. N.; Gorokhov, V. Yu.; Belitsky, G. M.; Vasin, A. V. *Diamond Relat. Mater.* **2000**, *9*, 792.

(4) Grill, A. *Diamond Relat. Mater*. **1999**, *8*, 428.

(5) Godet, C.; Conway, N. M. J.; Bourée, J. E.; Bouamra, K.; Grosman, A.; Ortega, C. *J. Appl. Phys.* **2002**, *91*, 4154 and references therein.

(6) Chaudhari, P.; Lacey, J.; Doyle, J.; Galligan, E.; Lien, S.-C. A.; Callegari, A.; et al. *Nature* **2001**, *411*, 56.

(7) Stöhr, J.; Samant, M. G.; Lüning, J.; Callegari, A. C.; Chaudhari, P.; Doyle, J. P.; Lacey, J. A.; Lien, S. A.; Purushothaman, S.; Speidell, J. L. *Science* **2001**, *292*, 2299.

(8) Reyes, R.; Legnani, C.; Ribeiro Pinto, P. M.; Cremona, M.; de Araújo, P. J. G.; Achete, C. A. *Appl. Phys. Lett.* **2003**, *82*, 4017.

(9) Lmimouni, K.; Legrand, C.; Dufour, C.; Chapoton, A.; Belouet, C. *Appl. Phys. Lett.* **2001**, *78*, 2437.

(10) Jacob, W. *Thin Solid Films* **1998**, *326*, 1.

(11) Gielen, J. W. A. M.; Kleuskens, P. R. M.; van de Sanden, M. C. M.; van IJzendoorn, L. J.; Schram, D. C.; Dekempeneer, E. H. A.; Meneve, J. *J. Appl. Phys.* **1996**, *80*, 5986.

(12) Gielen, J. W. A. M.; van de Sanden, M. C. M.; Schram, D. C. *Appl. Phys. Lett.* **1996**, *69*, 152.

(13) van de Sanden, M. C. M.; van Hest, M. F. A. M.; de Graaf, A.; Smets, A. H. M.; Letourneur, K. G. Y.; Boogaarts, M. G. H.; Schram, D. C. *Diamond Relat. Mater.* **1999**, *8*, 677.

(14) Engeln, R.; Letourneur, K. G. Y.; Boogaarts, M. G. H.; van de Sanden, M. C. M.; Schram, D. C. *Chem. Phys. Lett.* **1999**, *310*, 405.

(15) Benedikt, J.; Letourneur, K. G. Y.; Wisse, M.; Schram, D. C.; van de Sanden, M. C. M. *Diamond Relat. Mater.* **2002**, *11*, 989.

(16) Benedikt, J.; Wisse, M.; Woen, R. V.; Engeln, R.; van de Sanden, M. C. M. *J. Appl. Phys.* **2003**, *94*, 6932.

(17) Benedikt, J.; Woen, R. V.; van Mensfoort, S. L. M.; Perina, V.; Hong, J.; M van de Sanden, M. C. *Diamond Relat. Mater.* **2003**, *12*, 90.

(18) Gielen, J. W. A. M.; Kessels, W. M. M.; van de Sanden, M. C. M.; Schram, D. C. *J. Appl. Phys.* **1997**, *82*, 2643.

(19) de Graaf, A.; van Hest, M. F. A. M.; van de Sanden, M. C. M.; Letourneur, K. G. Y.; Schram, D. C. *Appl. Phys. Lett.* **1999**, *74*, 2927.

(20) Kessels, W. M. M.; van de Sanden, M. C. M.; Schram, D. C. *J. Vac. Sci. Technol., A* **2000**, *18*, 2153.

(21) Kessels, W. M. M.; van Assche, F. J. H.; Hong, J.; Schram, D. C.; van de Sanden, M. C. M. *J. Vac. Sci. Technol., A* **2004**, *22*, 96.

(22) Beulens, J. J.; de Graaf, M. J.; Schram, D. C. *Plasma Sources Sci. Technol.* **1993**, *2*, 180.

(23) van de Sanden, M. C. M.; de Regt, J. M.; Schram, D. C. *Plasma Sources Sci. Technol.* **1994**, *3*, 511.

(24) Smets, A. H. M.; Schram, D. C.; van de Sanden, M. C. M. *J. Appl. Phys.* **2000**, *88*, 6388.

(25) Benedikt, J.; Agarwal, S.; Eijkman, D. J.; Vandamme, W.; Creatore, M.; van de Sanden, M. C. M. *J. Vac. Sci. Technol., A* **2005**, *23*, 1400.

(26) Engeln, R.; Mazzouffre, S.; Vankan, P.; Schram, D. C.; Sadeghi, N. *Plasma Sources Sci. Technol.* **2001**, *10*, 595.

(27) Tsuji, M.; Kouno, H.; Matsumura, K.; Funatsu, T.; Nishimura, Y. *J. Chem. Phys*. **1993**, *98*, 2011.

(28) van de Sanden, M. C. M.; Severens, R. J.; Kessels, W. M. M.; Meulenbroeks, R. F. G.; Schram, D. C. *J. Appl. Phys.* **1998**, *84*, 2426.

(29) Derktatch, A. M.; Al-Khalili, A.; Vikor, L.; Neau, A.; Shi, W.; Danared, H.; af Ugglas, M.; Larsson, M. *J. Phys. B* **1999**, *32*, 3391.

(30) Janev, R. K.; Reiter, D. *Phys. Plasmas* **2002**, *9*, 4071.

(31) Janev, R. K.; Reiter, D. *Phys. Plasmas* **2004**, *11*, 780.

(32) van de Sanden, M. C. M.; de Regt, J. M.; Schram, D. C. *Plasma Sources Sci. Technol.* **1994**, *3*, 501.

(33) Kroesen, G. M. W.; Schram, D. C.; Wilbers, A. T. M.; Meeusen, G. J. *Contrib. Plasma Phys.* **1991**, *31*, 27.

(34) Chantry, P. J. *J. Appl. Phys.* **1987**, *62*, 1141.

(35) Perrin, J.; Shiratani, M.; Kae-Kune, P.; Videlot, H.; Jolly, J.; Guillon, J. *J. Vac. Sci. Technol*. **1998**, *16*, 278.

(36) Philipps, V.; Vietzke, E.; Flaskamp, K. *Surf. Sci*. **1986**, *178*, 806.

(37) Hopf, C.; Schwarz-Selinger, T.; Jacob, W.; von Keudell, A. *J. Appl. Phys.* **2000**, *87*, 2719.

(38) Neyts, E.; Bogaerts, A.; Gijbels, R.; Benedikt, J.; van de Sanden, M. C. M. *Diamond Relat. Mater*. **2004**, *13*, 1873.

(39) Laufer, A. H.; Fahr, A. *Chem. Rev.* **2004**, *104*, 2813.

(40) Ceursters, B.; Nguyen, H. M. T.; Peeters, J.; Nguyen, M. T. *Chem. Phys*. **2000**, *262*, 243.

(41) Stahl, F.; Schleyer, P. v. R.; Schaefer, H. F., III; Kaiser, R. I. *Planet. Space Sci.* **2002**, *50*, 685.

(42) Benedikt, J.; Eijkman, D. J.; Vandamme, W.; Agarwal, S.; van de Sanden, M. C. M. *Chem. Phys. Lett.* **2005**, *402*, 37.

(43) Kaiser, R. I.; Balucani, N.; Charkin, D. O.; Mebel, A. M. *Chem. Phys. Lett.* **2003**, *382*, 112.

(44) Angelova, G.; Novotny, O.; Mitchell, J. B. A.; Rebrion-Rowe, C.; Le Garrec, J. L.; Bluhme, H.; Seiersen, K.; Andersen, L. H. *Int. J. Mass Spectrom.* **2004**, *232*, 195.

(45) Nelson, H. H.; Helvajian, H.; Pasternack, L.; McDonald, J. R. *Chem. Phys.* **1982**, *73*, 431.

(46) Mebel, A. M.; Kaiser, R. I. *Chem. Phys. Lett.* **2002**, *360*, 139.

(47) Kaiser, R. I.; Ochsenfeld, C.; Head-Gordon, M.; Lee, Y. T.; Suits, A. G. *J. Chem. Phys.* **1997**, *106*, 1729.

(48) Rubio, M.; Stålring, J.; Bernhardsson, A.; Lindh, R.; Roos, B. O. *Theor. Chem. Acc.* **2000**, *105*, 15.

(49) Boullart, W.; Devriendt, K.; Borms, R.; Peeters, J. *J. Phys. Chem.* **1996**, *100*, 998.

(50) Vereecken, L.; Peeters, J. *J. Phys. Chem.* **1999**, *103*, 5523.

(51) Cartechini, L.; Bergeat, A.; Capozza, G.; Casavecchia, P.; Volpi, G. C.; Geppert, W. D.; Naulin, C.; Costes, M. *J. Chem. Phys.* **2002**, *116*, 5603.

(52) Baulch, D. L.; Cobos, C. J.; Cox, R. A.; Esser, C.; Frank, P.; Just, Th.; Kerr, J. A.; Pilling, M. J.; Troe, J.; Walker, R. W.; Warnatz, J. *J. Phys. Chem. Ref. Data* **1992**, *21*, 411.

(53) Mankelevitch, Yu. A.; Suetin, N. V.; Ashfold, M. N. R.; Boxford, W. E.; Orr-Ewing, A. J.; Smith, J. A.; Wills, J. B. *Diamond Relat. Mater*. **2003**, *12*, 383.

(54) von Keudell, A. *Thin Solid Films* **2002**, *402*, 1.

(55) Linstrom, P. J., Mallard, W. G., Eds. *NIST Chemistry WebBook*; NIST Standard Reference Database Number 69; National Institute of Standards and Technology: Gaithersburg, MD, 2003 (http://webbook.nist.gov).

(56) Owczarek, J. A. *Fundamentals of Gas Dynamics*; International Textbook: Scranton, PA, 1964.